# Computational Design of Rubber Balloons

Mélina Skouras[1]    Bernhard Thomaszewski[2]    Bernd Bickel[2]    Markus Gross[1,2]
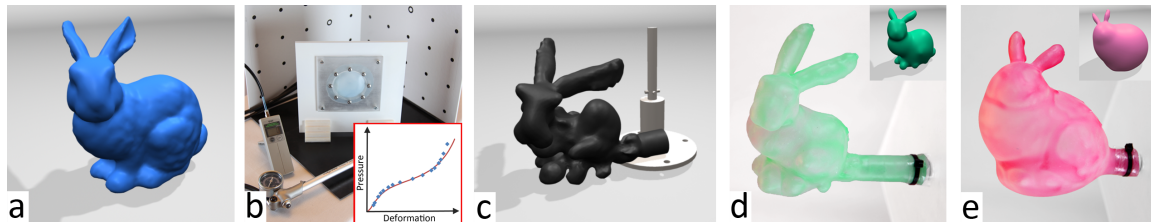
[1]ETH Zürich    [2]Disney Research Zurich



**Figure 1:** *Given a target shape (a), we use experimentally-acquired material properties (b) to compute and fabricate an optimal balloon shape (c). Upon inflation, the optimized balloon closely approximates the target (d), whereas inflating a small version of the target (e) results in poor approximation.*

## Abstract

*This paper presents an automatic process for fabrication-oriented design of custom-shaped rubber balloons. We cast computational balloon design as an inverse problem: given a target shape, we compute an optimal balloon that, when inflated, approximates the target as closely as possible. To solve this problem numerically, we propose a novel physics-driven shape optimization method, which combines physical simulation of inflatable elastic membranes with a dedicated constrained optimization algorithm. We validate our approach by fabricating balloons designed with our method and comparing their inflated shapes to the results predicted by simulation. An extensive set of manufactured sample balloons demonstrates the shape diversity that can be achieved by our method.*

## 1. Introduction

Inflatable balloons are fascinating objects that attract the attention of both children and adults. Especially rubber balloons enjoy a high popularity, be it for advertisement and decoration or simply as toys. Inflating a rubber balloon is a unique experience, but the diversity of existing balloon shapes is rather *deflating*: ellipsoids, wavy tubes, and coarse approximations of hearts and bunnies constitute a nearly exhaustive catalogue. The reason for this monotony is clearly not a lack of shapes that would make for exciting balloons. Indeed, computer graphics offers a large variety of tools and techniques for manipulating and synthesizing shapes through geometric design, real-world capture or physical simulation—we are inspired by the idea of leveraging this wealth for designing custom-shaped rubber balloons.

The fabrication process for standard rubber balloons is relatively simple: a positive mold, similar in shape to the inflated balloon, is briefly dipped into liquid rubber. The balloon is then cured, removed from the mold, and ready to deploy. Although this process would allow for more complex shaped molds, manually designing a mold that yields a desired inflated shape is a formidable task. By contrast, balloons made of plastic or aluminum foil can have more complex shapes, but they are more difficult to fabricate and do not stretch noticeably when inflated. Nevertheless, the large deformations observed during inflation are essential for the unique character of rubber balloons.

The goal of this work is to develop a method for designing balloons that, once fabricated, can be inflated into as complex shapes as foil balloons but are as deformable and as easy to manufacture as conventional rubber balloons. Solving this challenging problem requires knowledge and technologies from different fields, primarily constrained optimization, physical simulation, and computational material design. While our research would fit into any of these specific areas, computer graphics is actively contributing to all of them and thus, we believe, provides the best context for this work.

There are essentially two options for controlling the inflated shape of a balloon: varying its material properties locally and modifying its rest shape. Arbitrarily varying the material properties is technically very difficult, but controlling the stiffness by locally adapting the thickness of a homogeneous material seems feasible. Though promising at first, we found through experiments that this technique alone cannot provide sufficient shape variation. Furthermore, varying the thickness will most likely require a closed mold, which significantly complicates the fabrication process. In optimizing the rest shape, however, we can approximate a wide range of targets with constant-thickness material. Moreover, this process is amenable to dip molding fabrication. This together, we believe, is the enabling technology for practical fabrication of custom-shaped rubber balloons.

**Overview & Contributions** In this paper we present a method for automatic design and easy fabrication of balloons that can be inflated into desired shapes. We demonstrate on an extensive set of examples that our method is able to create balloons with a wide range of complex shapes. While the uninflated balloons produced by our method resemble their target shapes to some extent (see, e.g., Fig. 1), they are not mere down-scaled versions thereof and are very difficult to design manually. Our main contributions can be summarized as follows:

- We describe a complete process for designing and fabricating custom-shaped rubber balloons, including parameter acquisition, computational modeling, shape optimization and physical fabrication.
- We cast balloon shape optimization as a constrained minimization problem, combining strict enforcement of physical consistency with optimal shape approximation.
- We validate our method on a set of test cases and demonstrate its capabilities on a number of challenging balloon shapes.

## 2. Related Work

Computer graphics and related fields in physics and engineering have extensively studied the physical behavior of elastic materials and thin structures. In the following section, we only describe a small subset most relevant to the computational design of rubber balloons.

**Simulating** deformable surfaces has been a primary focus of computer animation ever since the early work of Terzopoulos et al. [TPBF]. Subsequent research has led to an abundant body of literature, of which we can only mention a few immediately related works. Wu et al. [WDGT01] simulate nonlinear membranes using finite elements. Volino et al. [VMTF09] use a membrane model derived from continuum mechanics for simulating cloth material. Grinspun et al. [GHDS] describe a discrete model for simulating thin shells. The mechanics of inflatable membranes have been

studied extensively in engineering (see [BWMH00] and references therein). In the context of computer vision, a simplified balloon model has been used for shape recovery and tracking [MT93]. However, fabrication-oriented design of balloons requires an accurate modeling of the material behavior of inflatable membranes. To our knowledge, this has not be considered in graphics before.

**Modeling and Fitting Materials** is crucial for accurate simulations. In the context of computer graphics, approaches were presented for estimating linear elastic material parameters [BT07], or nonlinear heterogeneous materials [BBO*b]. For deformable surfaces, Wang et al. [WOR] recently presented a parameter acquisition system for cloth.

**Rest Shape Optimization** is a highly relevant problem in various areas. In biomechanics, the effect of gravity and deformations induced by the scanning process has to be compensated to obtain an accurate model for simulation [PCG09]. In computer animation, artists create geometry already accounting for the effect of gravity. Derouet-Jourdan et al. [DJBDT] fit the parameters of a 2D dynamic rod model to match the shape of a given input curve. Twigg et al. [TKA] optimize the rest shape of mass spring systems to obtain sag-free simulations. Our application exhibits significantly larger deformations and external (pressure) forces that depend on the deformed geometry, making it a highly challenging optimization problem. In order to achieve art-directable solid simulations, Martin et al. [MTGG] introduce an additional elastic potential whose rest shape is chosen dynamically from a space of example poses.

**Fabrication-Oriented Design** has recently gained an increasing interest in graphics. Closely related is the design of foil balloons [FUM*] which are usually made out of aluminum. Compared to their rubber counterparts, foil balloons stretch very little and the inflated shapes are thus much easier to predict. In the broader context, various approaches for designing and fabricating plush toys [MI], paper craft models [MS], and burr puzzles [XLF*] have been presented. But also more general material properties such as appearance [HFM*, WPMR] and deformation behavior [BBO*a] have been investigated.

## 3. A Computational Model for Balloons

Our goal is to fabricate rubber balloons that, when inflated, assume a given target shape. To this end, we modify the rest shape of the balloons and use physical simulation to predict the resulting inflated shapes. This requires an adequate computational model, which is described in this section.

### 3.1. Mechanics

Rubber balloons can be inflated to several times their initial volume and still return to their original rest shape upon deflation. This observation suggests an elastic material model

and, due to the large deformations that are observed during inflation, we turn to nonlinear continuum mechanics.

The geometry of balloons, which are essentially thin layers of rubber, motivates a surface-centered representation. Accordingly, we describe the middle surface of the balloon in its undeformed and deformed configurations by the mappings $\bar{\mathbf{x}} : \Omega \subset \mathbb{R}^2 \to \mathbb{R}^3$, respectively $\mathbf{x} : \Omega \to \mathbb{R}^3$ with $\Omega \subset \mathbb{R}^2$ denoting the surface's parametric domain with coordinates $(u, v)$.

During inflation, balloons undergo both stretching and bending deformation. But unlike typical thin shell materials the in-plane deformation is extremely large such that the resulting forces can be assumed to overrule all bending contributions. Hence, the curvature of the surface is not important and only the stretching, i.e., the membrane deformation needs to be quantified. For this purpose, we start by introducing tangent vectors on the undeformed surface

$$\bar{\mathbf{a}}_u = \frac{\partial \bar{\mathbf{x}}}{\partial u} \,, \quad \text{and} \quad \bar{\mathbf{a}}_v = \frac{\partial \bar{\mathbf{x}}}{\partial v} \,, \tag{1}$$

and analogously define tangents $\mathbf{a}_u$ and $\mathbf{a}_v$ on the deformed surface. The inner products of the tangents give rise to the metric (or right Cauchy-Green) tensors $\bar{\mathbf{C}}$ and $\mathbf{C}$, which are symmetric $2 \times 2$ tensors whose components are defined as

$$\bar{\mathbf{C}}_{uv} = \bar{\mathbf{a}}_u^T \bar{\mathbf{a}}_v \,, \quad \text{respectively} \quad \mathbf{C}_{uv} = \mathbf{a}_u^T \mathbf{a}_v \,. \tag{2}$$

For simplicity, we will assume that the parameterization for the undeformed configuration is isometric such that $\bar{\mathbf{a}}_u$ and $\bar{\mathbf{a}}_v$ are orthonormal and $\bar{\mathbf{C}}$ is the $2 \times 2$ identity matrix, $\bar{\mathbf{C}} = \mathbf{I}$. This allows us to recover the familiar Green strain

$$\mathbf{E} = \tfrac{1}{2}(\mathbf{C} - \mathbf{I}) \,,$$

which is a $2 \times 2$ tensor describing the deformation of the balloon's middle surface. Although this measure does not explicitly account for deformations in the thickness direction, we can infer this information by introducing two *kinematic assumptions* [BWMH00]: First, the surface should not exhibit transverse shearing, and second, the deformation should be volume-preserving. The first requirement is part of the Kirchhoff-Love assumptions for thin shell models, while the second one accounts for the incompressible nature of rubber materials. Based on these assumptions, we construct a $3 \times 3$ metric tensor as

$$\hat{\mathbf{C}} = \begin{bmatrix} \mathbf{C}_{uu} & \mathbf{C}_{uv} & 0 \\ \mathbf{C}_{vu} & \mathbf{C}_{vv} & 0 \\ 0 & 0 & J^{-1} \end{bmatrix} \,, \tag{3}$$

where $J = \det \mathbf{C}$ is the determinant of the two-dimensional Cauchy Green tensor. This canonical strain representation is amenable to standard elastic material models, which are often described in terms of the first three invariants of $\hat{\mathbf{C}}$,

$$I_1 = \operatorname{tr}(\hat{\mathbf{C}}) \,, \quad I_2 = \frac{1}{2} \left[ I_1^2 - \operatorname{tr}(\hat{\mathbf{C}}^T \hat{\mathbf{C}}) \right] \,, \quad I_3 = \det \hat{\mathbf{C}} \,. \tag{4}$$

Assuming incompressibility, we have $I_3 = 1$ and can write the balloon's strain energy density $\Psi$ due to a given deformation $\hat{\mathbf{C}}$ as

$$\Psi(\hat{\mathbf{C}}) = \Psi(I_1, I_2) \,. \tag{5}$$

As part of our shape optimization process, we need to compute the equilibrium configuration that a balloon assumes under a certain internal pressure. If the air pressure inside the balloon is higher than on its outside, there is a resulting normal force density $\mathbf{f}^p$ acting in the outward direction of the balloon's surface. Neglecting gravity, static equilibrium implies that elastic and pressure force densities cancel out in every point on the surface, i.e.,

$$\frac{\partial \Psi(\mathbf{x})}{\partial \mathbf{x}} = -\mathbf{f}^p(\mathbf{x}). \tag{6}$$

### 3.2. Discretization

We use a finite element method for discretizing (6) in space and, following the assumptions of plane stress and negligible bending forces, settle for flat membrane elements, so called constant strain triangles (see, e.g., [Bat95]).

As a starting point, we approximate the geometry of a balloon with a closed triangle mesh with $n$ vertices whose deformed and undeformed positions we denote by $\mathbf{x}_i$ respectively $\bar{\mathbf{x}}_i$ for $1 \leq i \leq n$. Let $\bar{\mathbf{x}}_k^e$ and $\mathbf{x}_k^e$, $1 \leq k \leq 3$, denote the vertex positions pertaining to a given element $e$ and define corresponding edge vectors $\bar{\mathbf{e}}_{ij} = \bar{\mathbf{x}}_j^e - \bar{\mathbf{x}}_i^e$ and $\mathbf{e}_{ij} = \mathbf{x}_j^e - \mathbf{x}_i^e$. We endow the undeformed configuration with an orthonormal material frame $\bar{\mathbf{T}} = [\bar{\mathbf{u}} \, \bar{\mathbf{v}} \, \bar{\mathbf{d}}] \in \mathbb{R}^{3 \times 3}$, where

$$\bar{\mathbf{u}} = \frac{\bar{\mathbf{e}}_{12}}{|\bar{\mathbf{e}}_{12}|} \,, \quad \bar{\mathbf{d}} = \frac{\bar{\mathbf{u}} \times \bar{\mathbf{e}}_{13}}{|\bar{\mathbf{u}} \times \bar{\mathbf{e}}_{13}|} \,, \quad \bar{\mathbf{v}} = \bar{\mathbf{d}} \times \bar{\mathbf{u}} \,, \tag{7}$$

such that $\bar{\mathbf{u}}$ and $\bar{\mathbf{v}}$ span the plane of the element and $\bar{\mathbf{d}}$, the director, is its unit-length normal vector. Note that when using isotropic materials as in our case, the choice of the frame $\bar{\mathbf{u}}, \bar{\mathbf{v}}$ is not important and that frames do not have to be consistently oriented across elements. Consequently, there is no need for constructing (and tracking) a parametrization of the rest shape.

Since the deformation is assumed to be constant across each triangle, the geometry of a given deformed element is described by a single linear mapping $\mathbf{F}^e \in \mathbb{R}^{3 \times 3}$, the deformation gradient. We can conveniently integrate the kinematic assumptions from Sec. 3.1 into the definition of $\mathbf{F}^e$ by constraining the deformed director $\mathbf{d}$ as

$$\mathbf{d} = \frac{\mathbf{e}_{12} \times \mathbf{e}_{13}}{|\mathbf{e}_{12} \times \mathbf{e}_{13}|^2} \,. \tag{8}$$

This requires the deformed director to be normal to the deformed element (no transversal shear) and to be stretched such as to balance the change in area (incompressibility). We can now express the element's deformed geometry in terms of its undeformed state as

$$[\mathbf{e}_{12} \, \mathbf{e}_{13} \, \mathbf{d}] = \mathbf{F}^e \bar{\mathbf{T}}^{-1} [\bar{\mathbf{e}}_{12} \, \bar{\mathbf{e}}_{13} \, \bar{\mathbf{d}}] \,, \tag{9}$$

from which we obtain the deformation gradient as

$$\mathbf{F}^e = [\mathbf{e}_{12} \ \mathbf{e}_{13} \ \mathbf{d}] \left[ \bar{\mathbf{e}}_{12} \ \bar{\mathbf{e}}_{13} \ \bar{\mathbf{d}} \right]^{-1} \bar{\mathbf{T}} \ . \qquad (10)$$

See Fig. 2 for an illustration of these transformations. Note that the multiplication by $\bar{\mathbf{T}}$ aligns the material frame of the element such that the first two columns of $\mathbf{F}^e$ describe in-plane deformation while the third column corresponds to the thickness direction.
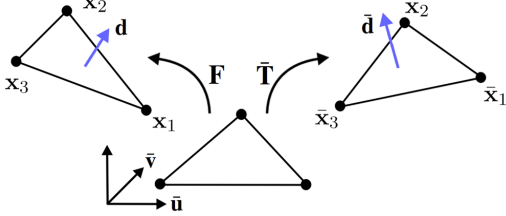


**Figure 2:** *Transformations between deformed (*left*), undeformed (*right*) and material (*middle*) domains for a membrane element.*

From the deformation gradient $\mathbf{F}^e$ we directly obtain the discrete Cauchy Green tensor $\mathbf{C}^e = (\mathbf{F}^e)^T \mathbf{F}^e$. Note that, by construction, $\mathbf{C}^e$ has the same special structure as its continuous counterpart in (3). Following the Total-Lagrangian finite element formulation [Bat95], we compute the elastic energy of a deformed element by integrating $\Psi$ over the undeformed domain. Since $\mathbf{C}^e$ is constant, we simply have

$$W^e(\mathbf{C}^e) = \int_{\bar{V}^e} \Psi(\mathbf{C}^e) \, dV = \Psi(\mathbf{C}^e) \cdot h \bar{A}_e \ , \qquad (11)$$

where $\bar{A}^e$ is the area of the undeformed element, $h$ the thickness of the balloon and $\bar{V}^e = h\bar{A}^e$. The total elastic energy of the balloon is obtained by summing up elemental contributions as $W = \sum_e W^e$.

**Pressure** The forces due to an enclosed pressurized gas tend to increase the volume of its container. Since the pressure is constant throughout the container, the resulting normal force density is the same everywhere on its surface. In the continuous setting, the pressure can be defined via the total forces $\mathbf{f}_A$ acting on a surface element $dA$ with normal $\mathbf{n}$ as

$$p = \lim_{dA \to 0} \frac{d\mathbf{f}_A \cdot \mathbf{n}}{dA} \ . \qquad (12)$$

This expression allows us to derive discrete nodal pressure forces as

$$\mathbf{f}_i^p = \sum_{j \in \mathcal{T}_i} w_{ij} \cdot p \cdot A_j \mathbf{n}_j \ , \qquad (13)$$

where $\mathcal{T}_i$ is the set of triangles incident to vertex $i$, $\mathbf{n}_j$ and $A_j$ are the area and normal of triangle $j$ and $w_{ij}$ are weights. We use constant weights of $w_{ij} = 1/3$, which is equivalent to computing the pressure forces from area-weighted normals.

As an aside, we note that the process of inflating a balloon is not a simple increase in pressure, but rather an increase in the number of gas molecules inside the balloon. The difference becomes clear when writing the ideal gas equation as

$$pV = NRT \ , \qquad (14)$$

where $N$ is the amount of gas contained in volume $V$, $T$ is the temperature and $R$ is the gas constant. Clearly, increasing the amount of gas (through pumping) increases the product of pressure and volume but neither of them has to increase monotonically.

**Numerical Solution** As part of our shape optimization (Sec. 5) and parameter fitting (Sec. 4) methods, we have to compute the deformed shape that a balloon assumes under a given inflation pressure. This is a static equilibrium problem which we solve by requiring nodal force balance, i.e.,

$$\mathbf{f}_k^{\text{mem}} + \mathbf{f}_k^p = \mathbf{0} \qquad k \in 0 \ldots 3n \ , \qquad (15)$$

where $\mathbf{f}_k^{\text{mem}} = -\nabla_{\mathbf{x}} W(\mathbf{x}_k)$ are elastic membrane forces and $\mathbf{f}_k^p$ denote the pressure forces as defined in (13). We solve (15) with a Newton-Raphson procedure coupled with line search and incremental loading on the pressure term for improved stability. This expressions for the membrane forces and their Jacobian (tangent stiffness matrix) are generated automatically using a computer algebra package.

## 4. Modeling Balloon Material

Rubbers generally show a nonlinear stress-strain response. However, the extreme deformations observed during balloon inflation lead to a particularly complex behavior which, as shown below, most conventional material models cannot properly reflect. But whatever the material model, it is crucial to determine its parameters experimentally in order to obtain accurate agreement with physical reality.

### 4.1. Measurements and Fitting

**Measurements** Similar to the system described by Treloar [Tre44], we fix a rubber membrane to the supporting plane of a base apparatus using a clamp with a circular opening of 6cm diameter (see Fig. 1 b). Two holes on the back of the supporting plane allow us to connect a valve and an off-the-shelf pump for inflation as well as a digital manometer. The measurement process for a given sample membrane consists of 10 loading steps in each of which we inject an additional (predefined) amount of air, record the resulting pressure and capture the deformed geometry using a standard laser scanner. We then determine the spatially averaged extension ratio $\rho_i^{\text{avg}}$ for step $i$ from the area of the reconstructed geometry $A_i$ as $\rho_i^{\text{avg}} = \sqrt{A_i/A_0}$.

Our method is not restricted to a particular type of rubber, but for practical reasons (see Sec. 6), we exclusively used silicone for fabrication. We performed tests for silicone membranes with four different thicknesses (0.25, 0.5, 0.75

and 1.0mm), using three samples per thickness value to account for fabrication tolerance. Fig. 3 shows the measured data (blue spades) for a thickness of 0.5mm averaged over the three samples.

**Fitting** With this set of measurements, we then determine the material coefficients of our computational model by minimizing the difference between simulated and captured shapes, using the optimization algorithm described in Sec. 5. Doing this simultaneously for all measured pressure values, we obtain material coefficients that provide the best average match for the entire deformation range of the experiment.

### 4.2. Evaluation

As can be seen from Fig. 3, the measurements reveal an unusual deformation behavior. The average extension ratio first increases almost linear with respect to the pressure. At a certain point, however, there is a clear inflection in the curve indicating a second deformation regime of the material. In a third regime, the material stiffness increases again.

Inflated balloons will in general exhibit inhomogeneous deformations, most likely covering all three regimes. If good approximations are to be obtained, then this particular behavior must be reproduced by the material model. We will discuss some candidates in the following and, in order to facilitate comparison, we provide stress-strain curves for all models considered in Fig. 3. The interested reader is referred to the textbook by Bonet and Wood [BW97] for details.
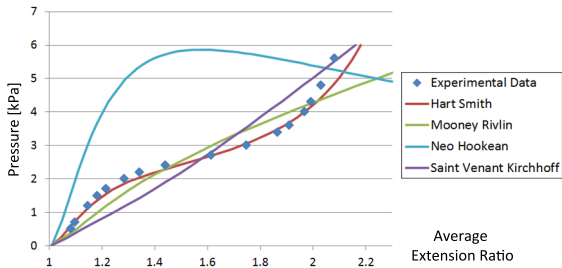


**Figure 3:** *Experimental data for the pressure-extension behavior of a silicone membrane and approximations with different material models.*

The membrane formulation described in Sec. 3 guarantees volume preservation through geometric assumptions (thickness stretch compensates change in area) and thus avoids the numerical problems typically associated with incompressible elasticity. In this setting, the simplest nonlinear material model is the Neo-Hookean solid, which describes the strain energy as a linear function of the first invariant $I_1$. However, as can be seen in Fig. 3, this model fails dramatically to approximate the deformation behavior of real rubber. The reason for this is that the Neo-Hookean material has a pressure

peak at a rather small extension ratio beyond which the pressure drops with increasing deformation. Visually speaking, the peak value has to be high enough to match the pressure values for larger extension ratios from the experimental data. But as a result, the overall deformation behavior deviates wildly from the experiment.

The second model that we considered is the St.Venant-Kirchhoff solid [BW97] which, despite shortcomings [ITF], is widely used in graphics. But while the approximation is significantly better than for the Neo-Hookean material, it cannot reproduce the three characteristic deformation regimes of the experimental data. A similar behavior is observed for the Mooney-Rivlin material, which is a generalization of the Neo-Hookean solid that also considers the second invariant $I_2$ (see [BW97]). One option to improve the approximation quality is to include higher powers of the invariants or resort to Ogden-type models [Ogd84], which describe the energy in terms of powers of the principal stretches. However, each additional term entails an additional material constant, which increases the model complexity and thus complicates the process of parameter fitting.

The experimental observations by Treloar [Tre44] suggest that, for large strains, rubber material exhibits an energy growth which is an exponential rather than a polynomial function of the invariants. The empirical model of Hart-Smith [HS66] takes this behavior directly into account, describing an exponential strain energy function through its derivatives as

$$\frac{\partial W}{\partial I_1} = G \cdot \exp(k_1(I_1 - 3)^2), \quad \frac{\partial W}{\partial I_2} = G \cdot \frac{k_2}{I_2}, \quad (16)$$

where $k_1$, $k_2$ and $G$ are material constants. Visually, the deformation behavior for small to moderate stretches is determined by $G$ and $k_2$, while $k_1$ decides how quickly the exponential growth manifests. Despite the small set of material coefficients, the Hart-Smith material is capable of accurately reproducing the three deformation regimes observed in the experimental data.

The elastic forces for the Hart-Smith model can be computed directly from (16) as

$$\mathbf{f}^{\text{mem}} = -\frac{\partial W}{\partial \mathbf{x}} = -\frac{\partial W}{\partial I_1}\frac{\partial I_1}{\partial \mathbf{x}} - \frac{\partial W}{\partial I_2}\frac{\partial I_2}{\partial \mathbf{x}}. \quad (17)$$

The derivatives of the two invariants can be calculated by hand when using (3) in (4) and deriving component-wise. But since the involved expressions are rather lengthy and thus prone to error, we opt for a computer algebra software to compute first and second derivatives of $W$ with respect to current as well as undeformed positions.

### 5. Shape Optimization

This section explains our strategy for computing optimal rest shapes for balloons, which we cast as a nonlinear constrained optimization problem. We start by formalizing the

problem, then proceed to its solution via constrained nonlinear optimization and finally address some additional technical aspects.

## 5.1. Problem Setting

Our goal is to find a rest shape that, upon inflation, approximates the target shape as closely as possible. We measure *closeness* in terms of a distance energy $E_{dist}(\hat{\mathbf{x}}, \mathbf{x})$ depending on the geometries of the inflated balloon, $\mathbf{x}$, and the target shape, $\hat{\mathbf{x}}$. The distance measure should capture differences in first (stretching) and second (bending) fundamentals forms between the inflated balloon and the target shape. We use a variant of the discrete shell energy by Grinspun et al. [GHDS] for this purpose and, using $\mathbf{x}$ and $\hat{\mathbf{x}}$ as current respectively rest state, define

$$E_{dist} = \sum_e \left[ k_l (1 - \frac{l_e}{l_e^0})^2 + k_b (\theta_e - \theta_e^0)^2 \right] l_e^0 , \qquad (18)$$

where $l_e$ and $\theta_e$ ($l_e^0$ and $\theta_e^0$) denote the deformed (undeformed) length and dihedral angle of edge $e$ and $k_l$, $k_b$ are stretching and bending coefficients. In comparison to simpler measures based on pairwise vertex distance, this metric has the advantage that the error caused by local deviations in shape remains local and does not propagate over the model.

With this distance metric established, we seek to find the physical solution, i.e., a configuration in force equilibrium, which is closest to the target shape, i.e., minimizes (18). These requirements can be formulated as a constrained optimization problem with an objective function

$$\Lambda(\bar{\mathbf{x}}, \mathbf{x}, \lambda) = E_{dist}(\hat{\mathbf{x}}, \mathbf{x}) - \lambda^t \mathbf{C}(\bar{\mathbf{x}}, \mathbf{x}) \qquad (19)$$

where $\mathbf{C}$ is a vector of constraints, each of which measures the deviation from force equilibrium for a given degree of freedom, i.e.,

$$\mathbf{C}_j(\bar{\mathbf{x}}, \mathbf{x}) = \mathbf{f}_j^{\text{mem}} + \mathbf{f}_j^{\text{p}} \qquad j = 1 \ldots 3n , \qquad (20)$$

Note that the system is in equilibrium only if $\mathbf{C}(\bar{\mathbf{x}}, \mathbf{x}) = \mathbf{0}$.

## 5.2. Numerical Solution

The problem described by (19) has a comparatively large number of constraints (as many as degrees of freedom) and we would like a method that can deal efficiently with this case. The two most widely used approaches for constrained optimization are sequential quadratic programming (SQP) and the penalty method [NW00]. Solving the problem with SQP breaks down to finding roots of the gradient of (19) using Newton's method. This promises accurate constraint satisfaction but also leads to large indefinite systems of equations which are costly to solve. The penalty method, by contrast, does not increase the dimension of the system but strict constraint satisfaction, mandatory in our case, leads to ill-conditioned systems and thus numerical problems. As a

hybrid between SQP and penalty methods, augmented Lagrangian methods (ALMs) strive to combine the advantages of both: they offer accurate constraint satisfaction without ill-conditioning (unlike the penalty method) but do not entail an increase in dimension (unlike SQP). ALMs are obtained by *augmenting* the Lagrangian of the constrained minimization problem (19) by an additional penalty term,

$$\Lambda = E_{dist}(\hat{\mathbf{x}}, \mathbf{x}) - \lambda^t \mathbf{C}(\bar{\mathbf{x}}, \mathbf{x}) + \frac{\mu}{2} ||\mathbf{C}(\bar{\mathbf{x}}, \mathbf{x})||^2 . \qquad (21)$$

This objective function is minimized iteratively in a sequence of unconstrained minimization and multiplier update steps. In the first step of a given iteration, the Lagrange multipliers are kept fixed and $\Lambda$ is minimized with respect to the free variables $\bar{\mathbf{x}}$ and $\mathbf{x}$ using a standard Newton-Raphson method with line search. Having solved the nonlinear system, we check whether the constraints have sufficiently decreased, in which case we update the Lagrange multipliers according to

$$\lambda_i = \lambda_i - \mu \mathbf{C}_i \qquad (22)$$

Otherwise, we increase the penalty coefficient $\mu$ and leave the multipliers unchanged. The iterations are stopped once the norm of the gradient (21) and the one of the constraint vector fall below given thresholds. We refer the reader to Nocedal and Wright [NW00] for a complete exposition of ALM and its implementation.

**Regularization** The problem described by (21) is nonlinear as well as nonconvex and will therefore exhibit local minima. In particular, any region on the rest shape enclosed by a planar curve can be mirrored without altering the inflated shape. In order to obtain a well-posed problem, we favor convex shapes by asking for the solution with maximum volume. A numerical problem arises in regions with coplanar elements, for which the hessian of the membrane energy exhibits a null-space in the normal direction. We solve this issue with an additional energy term based on the bending component of (18), thus penalizing curvature deviations from the initial rest shape.

**Inflation Pressure** The optimization process starts with a downscaled version of the target shape. For practical reasons, we do not directly prescribe an extension ratio between uninflated and inflated balloons but determine an inflation pressure which achieves the desired increase in volume. To this end, we first increase the inflation pressure in a sequence of static equilibrium solves, until the volume of the inflated shape matches the volume of the target shape. We then use this pressure to compute the optimal balloon shape.

**Parameter Fitting** We use the optimization process described above also for fitting material parameters to measured data, albeit with three modifications: first, we optimize for material parameters, not for rest shape positions. Second, we have targets described as pairs of pressure and corresponding geometry and we minimize the distance to all of

them simultaneously. Third, we use a different distance measure based on a smooth interpolation of the reconstructed geometry using radial basis functions (RBF). We define the corresponding energy as

$$E_{rbf}(\bar{\mathbf{x}}) = \frac{1}{2} \sum_i ||f(\bar{\mathbf{x}}_i)||^2 , \qquad (23)$$

where $f(\mathbf{x})$ is the function whose zero-level set defines the smooth RBF-surface (see Carr et al. [CBC*]).

**Rest Shape Intersections** If not explicitly prevented, the optimization process is likely to introduce intersections in the rest shapes. We use a collision handling strategy based on penalty forces to avoid such unphysical settings. In each iteration of the optimization, we first detect all pairs of vertices that are closer than a given threshold $\varepsilon_c$. In order to improve runtime performance, we use a kD-tree and cull vertex-pairs whose (approximate) geodesic distance is smaller than a threshold value $\varepsilon_{gd}$. For each vertex pair $(\bar{\mathbf{x}}_i, \bar{\mathbf{x}}_j)$ returned by the detection step, we introduce a penalty potential as

$$W_p(\bar{\mathbf{x}}_i, \bar{\mathbf{x}}_j) = (|\bar{\mathbf{x}}_i - \bar{\mathbf{x}}_j| - \varepsilon_c)^3 , \qquad (24)$$

which is active for $|\bar{\mathbf{x}}_i - \bar{\mathbf{x}}_j| - \varepsilon_c < 0$ and set to zero otherwise. Note that the cubic power of the potential ensures continuity of its second derivatives. The potentials for all points are then added to (19) such that, upon convergence, all vertex-vertex constraints are satisfied. Although this simple approach cannot resolve all intricate collisions in general, we found it to be sufficient for all our examples.

**Nozzle Attachment** We endow each balloon with a nozzle for inflation which we attach to the geometry of the rest shapes. We enforce the optimization to leave the attached geometry unchanged by imposing a set of corresponding position constraints.

## 6. Fabrication

The optimization method returns a triangle mesh for the balloon's rest shape. We complete the balloon mold by attaching a cylindrical tube to the previously defined nozzle vertices. We fabricate the mold on a 3D printer (Objet Connex 350), using a soft material to facilitate unmolding. See Fig. 1 (c) for an illustration.

Industrial balloon fabrication usually relies on latex due to its durability and low material costs. For manual fabrication, however, we found silicone more convenient to handle: unlike latex, it is not sensitive to temperature, cures without volume loss and can be evacuated to remove air inclusions. The silicone has to be mixed with an activator and be processed rapidly. Since remains cannot be stored, a dip-molding process is not attractive and we simply brush the rubber onto the mold. We then put the coated mold in a vacuum chamber to remove air inclusions. We found that this also leads to smoother coatings.

The coating thickness obtained by this process is in the range of 0.25mm-0.3mm. In order to increase the durability of the balloons we add another another layer using the same process. Finally, the balloon needs to cure for one day before removing it from the mold and an additional 5 to 7 days to obtain its final material properties.

## 7. Results

In order to explore the capabilities of our method we experimented with a variety of different target shapes. For each example, we computed an optimized rest shape, printed corresponding molds and fabricated the balloons using silicone. For comparison, we also fabricated balloons corresponding to the downscaled target shapes. Fig. 4 shows all results in a compact overview.

The last column clearly indicates that the downscaled targets do not lead to acceptable approximations. Indeed, the original shape is indiscernible in most cases. By contrast, the simulated shapes of the optimized balloons (col. 3) as well as the fabricated counterparts (col. 4) are in good agreement with the targets for the majority of the examples and most of the characteristic features are clearly discernible.

Comparing the target shapes against the simulated inflated balloons, several observations can be made. First, flat regions are not accurately reproduced since the pressure forces tend to push them outwards. This effect is clearly visible for the faces of the cube (row 2) but can also be identified on the legs of the elephant (row 5) and the arms of the armadillo (row 6). Furthermore, sharp transitions such as the borders around the bumps on the sphere (row 1) or the edges of the cube (row 2) remain visible but are smoothed out. However, isolated sharp features such as the corners of the cube can be reproduced with fair accuracy since they do not have to stretch during inflation and can thus be built into the undeformed shape. Finally, high frequency detail such as the fur of the bunny is lost. This is partly due to the limited accuracy of the fabrication process, but also owed to the fact that balloons cannot have local concave features since these would be *popped out* by the pressure forces. This observation also explains why the snout of the armadillo and the ears of the bunny (row 4) are rather roundish.

As a side note, it can be seen from the cube and the sphere example that our method preserves the overall symmetry of optimized shapes for symmetric targets, even for non-symmetric (irregular) meshes.

The inflated real balloons are in good agreement with their simulated counterparts, only the armadillo and the hand (row 7) examples show significant deviations. Parts of this effect could be due to approximations made in the material model, the mechanical model, and the numerics. However, the largest factor are most likely the inaccuracies in the fabrication process: the highly viscous silicone tends to accumulate in the troughs of the complex-shaped molds, leading to
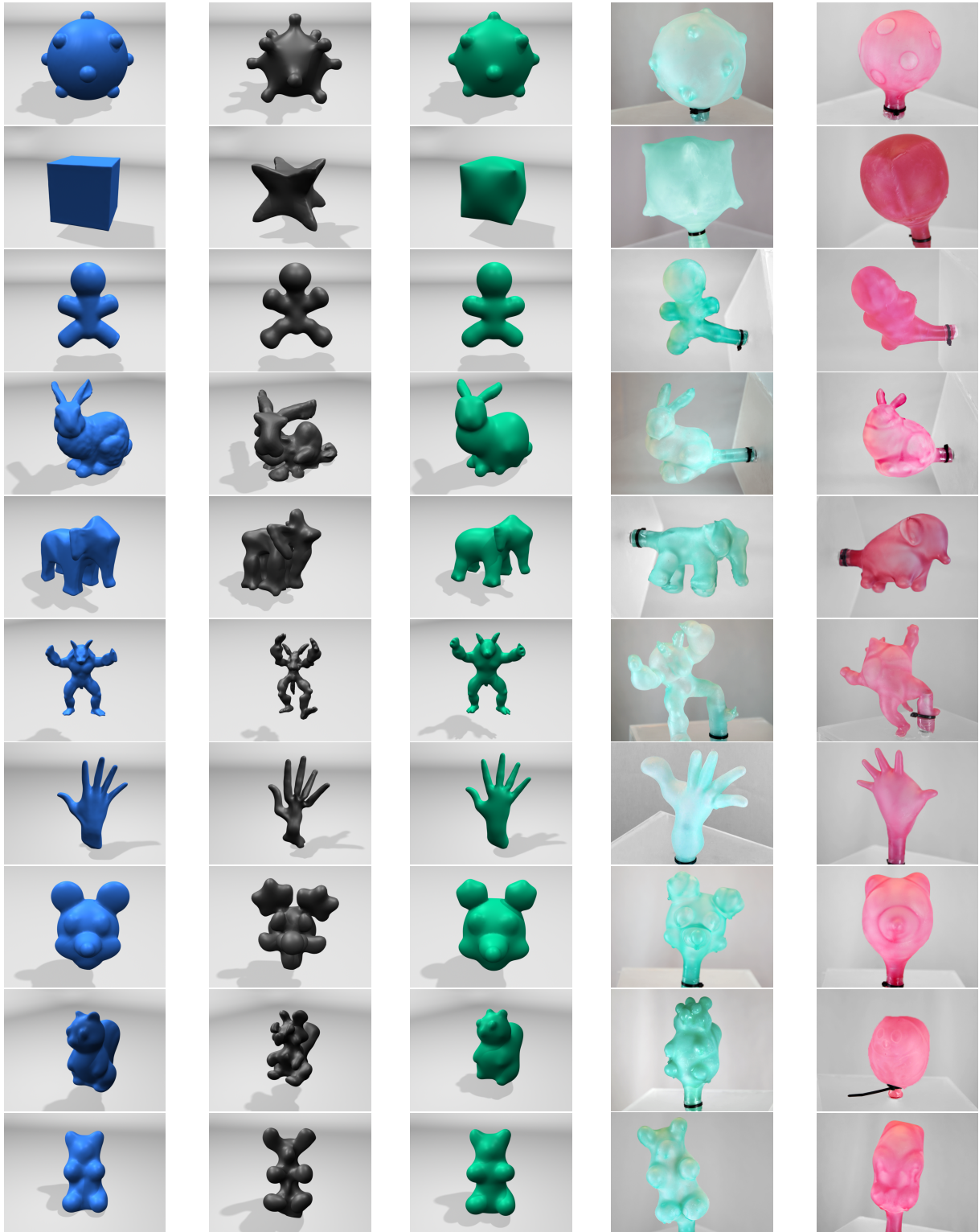
**Figure 4:** *Results obtained with our method. The columns (from left to right) show target shapes, optimized balloons, simulated inflated balloons, fabricated optimized balloons and fabricated balloons corresponding to downscaled targets.*

significant thickness variations. This effect could be reduced by using thinned rubber and a higher number of layers, albeit at the expense of increased fabrication times.

**Larger Inflations** The average extension ratio for the inflated balloons stays below 2.5 in all examples since the silicone would soon rupture for larger deformations. Nevertheless, extension ratios of around 5 are often observed for latex balloons. But while our particular choice of material limits the increase in volume, this limitation is not inherent to our approach: we simulate a standard balloon with a latex material whose parameters we determined in the same way as for silicone (Fig. 5, left). Using latex, we can attain extension ratios larger than 5 as shown in the example on the right of Fig. 5. This also attests to the consistency of the optimization: our method yields an optimized balloon that closely resembles the original shape used to generate the inflated target. We also performed experiments with the latex material on more complex shapes such as the bear and obtained similar extension ratios (see accompanying video).
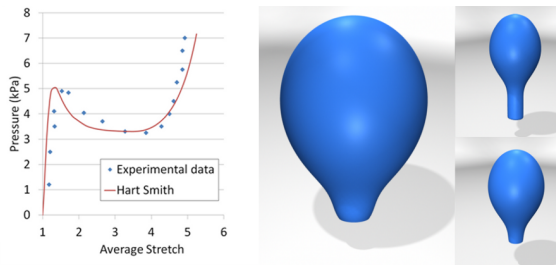


**Figure 5:** Left*: measured data for a latex membrane and the Hart-Smith model fit. Right: the inflated shape (left) of a standard latex balloon is used as a target in our optimization method. The resulting balloon shape (bottom-right) is close to the original shape (top-right).*

**Performance** We provide computation times for all examples shown in this paper in Table 1. It can be seen that for most balloons, our method takes less than 15 minutes to compute optimized shapes. With slightly less than 90 minutes, the bunny example takes by far the longest time to finish, which is mostly due to the large number of intersections that slow down convergence.

**Accuracy & Validation** In order to quantify the accuracy of our optimization method, we measured the difference between input target shapes and simulated optimized shapes. Fig. 6 shows an error plot for the bunny example using the distance metric of (18). For easier interpretation, we measured for each vertex of the inflated shape the distance to the closest point on the target surface, leading to an average/maximum error of 0.23/0.89cm (the inflated balloon has a maximum inter-vertex distance of 14.6cm). As expected, the regions of highest error coincide with those of minimal mean curvature.
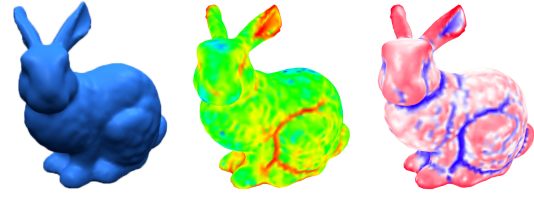


**Figure 6:** *Approximation error for the bunny with green/red indicating lowest/highest error (*middle*). Red/blue color indicates positive/negative mean curvature (*right*).*

To estimate the impact of the inaccuracies in the fabrication process, we applied random thickness perturbations of different magnitudes to the bunny model and investigated the impact on the inflated shape using again the vertex-based distance measure. A variation of 10% led to an average deviation of 0.22cm, whereas 20% of variation already results in 0.52cm average error. This agrees with our observations: small thickness variations have only little effect while larger variations such as as those seen in the armadillo and the hand example can lead to significant shape deviations.

We furthermore verified the importance of the material model experimentally. In a simple test, we compared the inflated shape of a real bunny balloon to the results produced by simulations using the Mooney-Rivlin and the Hart-Smith material. Fig. 1 (e) shows that the Hart-Smith material results in good approximation with clearly visible ears, whereas these features were not discernible for the Mooney-Rivlin material, which led to an almost spherical shape.

Finally, we analyzed the stability of the numerical solutions computed by our method. Using the bear example, we let our algorithm run on a perturbed version of the optimized rest shape and compared the result to the original solution. For an average vertex displacement of 0.25cm, the difference was below $10^{-4}$cm. This indicates that minima are well separated and we found this to be true for all examples considered.

| Model | #vertices | $t_{stat}$ [ms] | $t_{nwtn}$ [ms] | $t_{tot}$ [s] | #its |
|---|---|---|---|---|---|
| Armadillo | 6027 | 24494 | 5897 | 569 | 81 |
| Bumpsphere | 3265 | 20359 | 2993 | 201 | 55 |
| Bunny | 4975 | 61138 | 7212 | 5000 | 879 |
| Cube | 5153 | 39094 | 6543 | 243 | 20 |
| Elephant | 3818 | 26317 | 3031 | 3060 | 131 |
| Gingerbread | 2238 | 5329 | 1776 | 66 | 29 |
| Hand | 2253 | 24403 | 2696 | 3229 | 1137 |
| Mouse | 2633 | 22277 | 3200 | 627 | 180 |
| Squirrel | 5995 | 151447 | 7744 | 105 | 103 |
| Teddy | 3527 | 85936 | 3492 | 484 | 106 |

**Table 1:** *Computation times breakdown: static equilibrium (*$t_{stat}$*), a single Newton step (*$t_{nwtn}$*), total computation time (*$t_{tot}$*) and number of ALM iterations (#its).*

## 8. Limitations & Future Work

This paper presented a method for computational design of rubber balloons with desired inflated shapes. Our approach drastically increases the space of possible balloon shapes and we have demonstrated its capabilities on a set of challenging examples.

Although our method is able to produce a large variety of shapes, certain features are very difficult to reproduce, in particular flat parts, locally-bounded concave regions, and sharp edges. These limitations do, however, apply to rubber balloons in general and are not specific to our method.

There are evidently shapes that can be well-approximated by our method while others are difficult to reproduce with satisfying quality. However, many of these difficult shapes can be changed into models that lend themselves well to balloon fabrication—see, e.g., the elephant. Currently, we rely on artists to design geometrically similar but feasible target shapes. For future work, we would like to develop a method for automating this shape abstraction process.

**References**

[Bat95] BATHE K.-J.: *Finite Element Procedures*. Prentice Hall, 1995. 3, 4

[BBO*a] BICKEL B., BÄCHER M., OTADUY M. A., LEE H. R., PFISTER H., GROSS M., MATUSIK W.: Design and fabrication of materials with desired deformation behavior. In *Proc. of ACM SIGGRAPH '10*. 2

[BBO*b] BICKEL B., BÄCHER M., OTADUY M. A., MATUSIK W., PFISTER H., GROSS M.: Capture and modeling of nonlinear heterogeneous soft tissue. In *Proc. of ACM SIGGRAPH '09*. 2

[BT07] BECKER M., TESCHNER M.: Robust and efficient estimation of elasticity parameters using the linear finite element method. In *SimVis* (2007), pp. 15–28. 2

[BW97] BONET J., WOOD R. D.: *Nonlinear Continuum Mechanics for Finite Element Analysis*. Cambridge Univ. Press, 1997. 5

[BWMH00] BONET J., WOOD R., MAHANEY J., HEYWOOD P.: Finite element analysis of air supported membrane structures. *Comp. Meth. Appl. Mech. Engrg 190*, 5 (2000), 579–595. 2, 3

[CBC*] CARR J. C., BEATSON R. K., CHERRIE J. B., MITCHELL T. J., FRIGHT W. R., MCCALLUM B. C., EVANS T. R.: Reconstruction and representation of 3d objects with radial basis functions. In *Proc. of ACM SIGGRAPH '01*. 7

[DJBDT] DEROUET-JOURDAN A., BERTAILS-DESCOUBES F., THOLLOT J.: Stable inverse dynamic curves. In *Proc. of ACM SIGGRAPH Asia '10*. 2

[FUM*] FURUTA Y., UMETANI N., MITANI J., IGARASHI T., FUKUI Y.: A film balloon design system integrated with shell element simulation. In *EUROGRAPHICS 2010 short paper*. 2

[GHDS] GRINSPUN E., HIRANI A. N., DESBRUN M., SCHRÖDER P.: Discrete shells. In *Proc. of Symp. on Computer Animation (SCA '03)*. 2, 6

[HFM*] HAŠAN M., FUCHS M., MATUSIK W., PFISTER H., RUSINKIEWICZ S.: Physical reproduction of materials with specified subsurface scattering. In *Proc. of ACM SIGGRAPH '10*. 2

[HS66] HART-SMITH L. J.: Elasticity parameters for finite deformations of rubber-like materials. *Z. angew. Math. Phys. 17* (1966). 5

[ITF] IRVING G., TERAN J., FEDKIW R.: Invertible finite elements for robust simulation of large deformation. In *Proc. of Symp. on Computer Animation (SCA '04)*. 5

[MI] MORI Y., IGARASHI T.: Plushie: An interactive design system for plush toys. In *Proc. of ACM SIGGRAPH '07*. 2

[MS] MITANI J., SUZUKI H.: Making papercraft toys from meshes using strip-based approximate unfolding. In *Proc. of ACM SIGGRAPH '04*. 2

[MT93] MCINERNEY T., TERZOPOULOS D.: A finite element model for 3d shape reconstruction and nonrigid motion tracking. In *Proc. 4th Int. Conf. Computer Vision* (1993), pp. 518–523. 2

[MTGG] MARTIN S., THOMASZEWSKI B., GRINSPUN E., GROSS M.: Example-based elastic materials. In *Proc. of ACM SIGGRAPH '11*. 2

[NW00] NOCEDAL J., WRIGHT S. J.: *Numerical Optimization*. Springer, 2000. 6

[Ogd84] OGDEN R.: *Non-linear elastic deformations*. Ellis Horwood, 1984. 5

[PCG09] PATHMANATHAN P., CHAPMAN S., GAVAGHAN D.: Inverse membrane problems in elasticity. *Q. J. Mech. Appl. Math. 62*, 1 (2009), 67–87. 2

[TKA] TWIGG C. D., KAČIĆ-ALESIĆ Z.: Optimization for sag-free simulations. In *Proc. of Symp. on Computer Animation (SCA '11)*. 2

[TPBF] TERZOPOULOS D., PLATT J., BARR A., FLEISCHER K.: Elastically deformable models. In *Proc. of ACM SIGGRAPH '87*. 2

[Tre44] TRELOAR L. R. G.: Stress-strain data for vulcanised rubber under various types of deformation. *Trans. Faraday Soc. 40*, 59 (1944). 4, 5

[VMTF09] VOLINO P., MAGNENAT-THALMANN N., FAURE F.: A simple approach to nonlinear tensile stiffness for accurate cloth simulation. *ACM Trans. Graph. 28* (2009), 105:1–105:16. 2

[WDGT01] WU X., DOWNES M. S., GOKTEKIN T., TENDICK F.: Adaptive nonlinear finite elements for deformable body simulation using dynamic progressive meshes. *Comput. Graphics Forum (Proc. Eurographics) 20*, 3 (2001), 349–358. 2

[WOR] WANG H., O'BRIEN J. F., RAMAMOORTHI R.: Data-driven elastic models for cloth: Modeling and measurement. In *Proc. of ACM SIGGRAPH '11*. 2

[WPMR] WEYRICH T., PEERS P., MATUSIK W., RUSINKIEWICZ S.: Fabricating microgeometry for custom surface reflectance. In *Proc. of ACM SIGGRAPH '09*. 2

[XLF*] XIN S., LAI C.-F., FU C.-W., WONG T.-T., HE Y., COHEN-OR D.: Making burr puzzles from 3D models. In *Proc. of ACM SIGGRAPH '11*. 2